




## Article

# Palaeoecological Implications of Lower-Middle Triassic Stromatolites and Microbe-Metazoan Build-Ups in the Germanic Basin: Insights into the Aftermath of the Permian–Triassic Crisis

Yu Pei <sup>1,\*</sup>, Hans Hagdorn <sup>2</sup> , Thomas Voigt <sup>3</sup>, Jan-Peter Duda <sup>4,5</sup>  and Joachim Reitner <sup>1,5</sup> 

- <sup>1</sup> Geoscience Center, Department of Geobiology, Georg-August-Universität Göttingen, 37077 Göttingen, Germany; jreitne@gwdg.de
- <sup>2</sup> Muschelkalkmuseum, 74653 Ingelfingen, Germany; encrinus@hagdorn-ingelfingen.de
- <sup>3</sup> Institute of Geosciences, Friedrich-Schiller-Universität Jena, 07749 Jena, Germany; thomas.voigt@uni-jena.de
- <sup>4</sup> Sedimentology & Organic Geochemistry Group, Department of Geosciences, Eberhard Karls Universität Tübingen, 72076 Tübingen, Germany; jan-peter.duda@geo.uni-tuebingen.de
- <sup>5</sup> ‘Origin of Life’ Group, Göttingen Academy of Sciences and Humanities, 37073 Göttingen, Germany
- \* Correspondence: yu.pei@geo.uni-goettingen.de



**Citation:** Pei, Y.; Hagdorn, H.; Voigt, T.; Duda, J.-P.; Reitner, J. Palaeoecological Implications of Lower-Middle Triassic Stromatolites and Microbe-Metazoan Build-Ups in the Germanic Basin: Insights into the Aftermath of the Permian–Triassic Crisis. *Geosciences* **2022**, *12*, 133. <https://doi.org/10.3390/geosciences12030133>

Academic Editors: Michele Morsilli, Marcello Minzoni and Jesus Martinez-Frias

Received: 13 January 2022

Accepted: 9 March 2022

Published: 14 March 2022

**Publisher’s Note:** MDPI stays neutral with regard to jurisdictional claims in published maps and institutional affiliations.



**Copyright:** © 2022 by the authors. Licensee MDPI, Basel, Switzerland. This article is an open access article distributed under the terms and conditions of the Creative Commons Attribution (CC BY) license (<https://creativecommons.org/licenses/by/4.0/>).

**Abstract:** Following the end-Permian crisis, microbialites were ubiquitous worldwide. For instance, Triassic deposits in the Germanic Basin provide a rich record of stromatolites as well as of microbe-metazoan build-ups with nonspicular demosponges. Despite their palaeoecological significance, however, all of these microbialites have only rarely been studied. This study aims to fill this gap by examining and comparing microbialites from the Upper Buntsandstein (Olenekian, Lower Triassic) and the lower Middle Muschelkalk (Anisian, Middle Triassic) in Germany. By combining analytical petrography (optical microscopy, micro X-ray fluorescence, and Raman spectroscopy) and geochemistry ( $\delta^{13}\text{C}_{\text{carb}}$ ,  $\delta^{18}\text{O}_{\text{carb}}$ ), we show that all the studied microbialites formed in slightly evaporitic environments. Olenekian deposits in the Jena area and Anisian strata at Werbach contain stromatolites. Anisian successions at Hardheim, in contrast, host microbe-metazoan build-ups. Thus, the key difference is the absence or presence of nonspicular demosponges in microbialites. It is plausible that microbes and nonspicular demosponges had a mutualistic relationship, and it is tempting to speculate that the investigated microbial-metazoan build-ups reflect an ancient evolutionary and ecological association. The widespread occurrence of microbialites (e.g., stromatolites/microbe-metazoan build-ups) after the catastrophe may have resulted from suppressed ecological competition and the presence of vacant ecological niches. The distribution of stromatolites and/or microbe-metazoan build-ups might have been controlled by subtle differences in salinity and water depth, the latter influencing hydrodynamic processes and nutrient supply down to the microscale. To obtain a more complete picture of the distribution of such build-ups in the earth’s history, more fossil records need to be (re)investigated. For the time being, environmental and taphonomic studies of modern nonspicular demosponges are urgently required.

**Keywords:** Upper Buntsandstein; Middle Muschelkalk; nonspicular (“keratose”) demosponges; end-Permian mass extinction; microbialite; ecological niche; elevated salinity; palaeoenvironment; geobiology

## 1. Introduction

Microbialites represent benthic microbial communities (i.e., biofilms or microbial mats) fossilized through trapping and binding of detrital sediment and/or localized mineral precipitation [1–4]. Dating as far back as ca. 3.5 billion years ago (e.g., [5–7]), they were abundant during most of the Precambrian. In the Phanerozoic, they showed a marked decline [4], although the concept of decline is considered too simplistic [8]. However, microbialites display marked reoccurrences at certain times in the Phanerozoic, as for instance

in the aftermath of the Permian–Triassic crisis (e.g., [9–19]). The temporary proliferation of biofilms/microbial mats in this critical interval likely resulted from a suppressed ecological competition and/or seawater chemistry at that time [2,3,20].

Depending on their characteristics, microbialites can be classified into different types (e.g., stromatolites, thrombolites, dendrolites, and leiolites: [1,21–24]). Among these, stromatolites are particularly important. The name derives from the term ‘Stromatolith’, which was coined by Kalkowsky [21] to describe layered carbonate structures in the Lower Triassic Buntsandstein of central Germany. Importantly, this term does not consider the nature of biofilms or microbial mats. In fact, the microbial communities involved in stromatolite formation may range from phototrophs (e.g., cyanobacteria) (e.g., [25–28]) to light-independent chemolithotrophic or heterotrophic microbes (e.g., [29–33]). Particularly noteworthy are stromatolites formed by syntrophic consortia of anaerobic methane-oxidizing archaea and sulfate-reducing bacteria [34–37].

Recently, a new type of bioconstruction formed by microbes and metazoans (mainly nonspicular demosponges) was discovered [38,39] and termed microbe-metazoan build-ups [40]. Similar structures were described before in ancient rocks but not identified as nonspicular (“keratose”) demosponges [41,42]. ‘Reticular fabrics’ in microbialites from the Middle Muschelkalk *Diplopora* Dolomite of South Poland were generally related to sponges but not further specified [43]. Furthermore, Lower Triassic metazoan reefs from the western USA were attributed to non-specified sponges [44–46]. This implies that build-ups with nonspicular demosponges are perhaps more widespread than currently thought. One problem in the search for fossils of these organisms might be that they do not have spicules and possess hardly identifiable morphological characteristics. After relatively robust criteria for the identification of nonspicular demosponges in ancient records were established, and the presence of these organisms in Phanerozoic microbe-metazoan build-ups was demonstrated [38,39], several additional occurrences have been reported from early Neoproterozoic–Palaeogene successions worldwide [16,40,47–52].

In the Lower and Middle Triassic, the Germanic Basin recorded at least four intervals of major microbialite development, namely (i) in the Lower Buntsandstein [21,53], (ii) in the Upper Buntsandstein [54], (iii) in the Middle Muschelkalk [55–59], and (iv) in the Lower Keuper [60,61]. Recently, it was reported that some of the microbialites from the Middle Muschelkalk were associated with nonspicular demosponges [39,40]. Despite their significance for understanding the aftermath of the Permian–Triassic crisis, these microbialites have only rarely been studied. We aim to fill this gap by examining and comparing microbialites from other strata, including the Upper Buntsandstein (Olenekian, Lower Triassic) and the lower Middle Muschelkalk (Anisian, Middle Triassic). Based on our findings, palaeoecological implications of these records are further discussed.

## 2. Geological Setting

The Permian–Triassic Germanic Basin stretched across large areas of Central Europe. During these times, the basin was situated on the edge of the subtropical Tethys Ocean (Meliata Ocean) [62–64] (Figure 1). In the Olenekian (Early Triassic), it was connected to the Tethys Ocean systems through the East Carpathian Gate (ECG). During the Anisian (Middle Triassic), it was additionally linked by the Silesian–Moravian Gate (SMG) and the Western Gate (WG) [63,65]. Palaeogeographically, the three studied sections (the Jena area, Werbach, and Hardheim) were located between the Rhenish Massif (RM) and the Vindelician–Bohemian–Massif (VBM) (Figure 1).

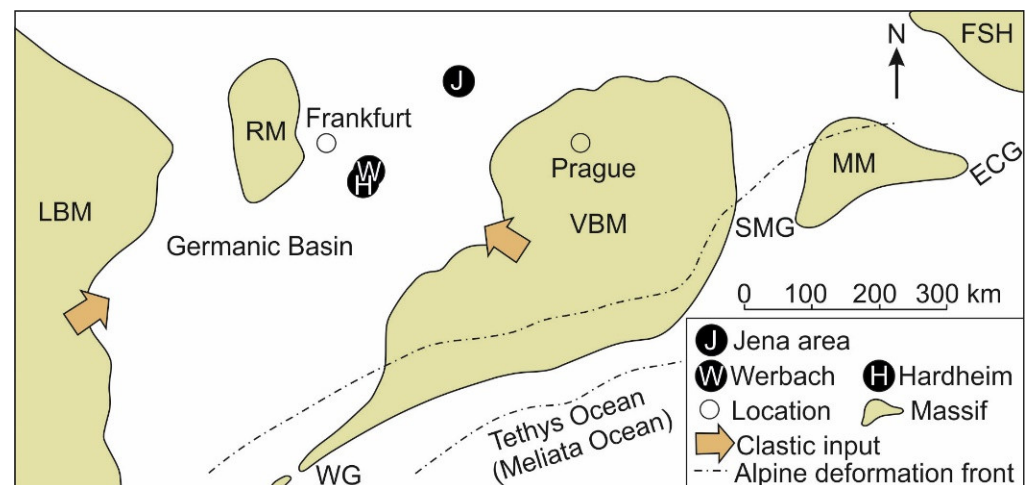


**Figure 1.** Palaeogeographic map of the Germanic Basin during the Triassic [62–65]. During the Olenekian (Early Triassic), the Germanic basin was connected to the Tethys (Meliata Ocean) through the East Carpathian Gate (ECG). During the Anisian (Middle Triassic), the Germanic Basin and the Tethys Ocean systems were additionally linked through the Silesian–Moravian Gate (SMG) and the Western Gate (WG). The three studied sections (Jena area, J; Werbach, W; Hardheim, H) were located between the Rhenish Massif (RM) and the Vindelician–Bohemian–Massif (VBM). LBM = London–Brabant–Massif. MM = Malopolska Massif. FSH = Fenno–Scandian High.

Sedimentary rocks from the Jena area ( $50^{\circ}52'36.03''$  N,  $11^{\circ}35'15.84''$  E, Thuringia, central Germany) belong to the Lower Röt Formation (Upper Buntsandstein Subgroup, Olenekian, Lower Triassic). The rocks consist of evaporites, marls, and muddy sandstones that are intercalated with dolomites and bioclastic limestones (Figure 2). The *Tenuis*-bank at the lower part of the section (SU 3) contains specimens of the ammonoid *Beneckeia tenuis*, the earliest Triassic ammonoid in the Germanic Basin, and is followed by stromatolites (Figure 2). The investigated stromatolites from the Werbach quarry ( $49^{\circ}39'54.38''$  N,  $9^{\circ}39'47.91''$  E, Baden–Württemberg, Southwest Germany) occur in the Geislingen Bed, a supraregional marker horizon [66] in the lower part of the Karlstadt Formation of the Middle Muschelkalk Subgroup (Anisian, Middle Triassic) (Figure 2). From bottom to top, the section can be subdivided into the Karlstadt, the Heilbronn and the Diemel Formations. The Karlstadt Formation is composed of dolomites, dolomitic marls, and dolomitic limestones. In addition to stromatolites, it locally contains fossils of organisms that inhabit elevated saline environments. The Heilbronn Formation with anhydrite and gypsum is almost devoid of any fossils. The Diemel Formation consists of dolomitic limestones and locally contains euryhaline faunas [66]. The microbe–metazoan build-ups exposed in the abandoned quarry near Hardheim ( $49^{\circ}36'2.23''$  N,  $9^{\circ}29'9.21''$  E, Baden–Württemberg, Southwest Germany) occur on top of the Geislingen Bed and are stratigraphically correlated with the stromatolites in the Werbach section.

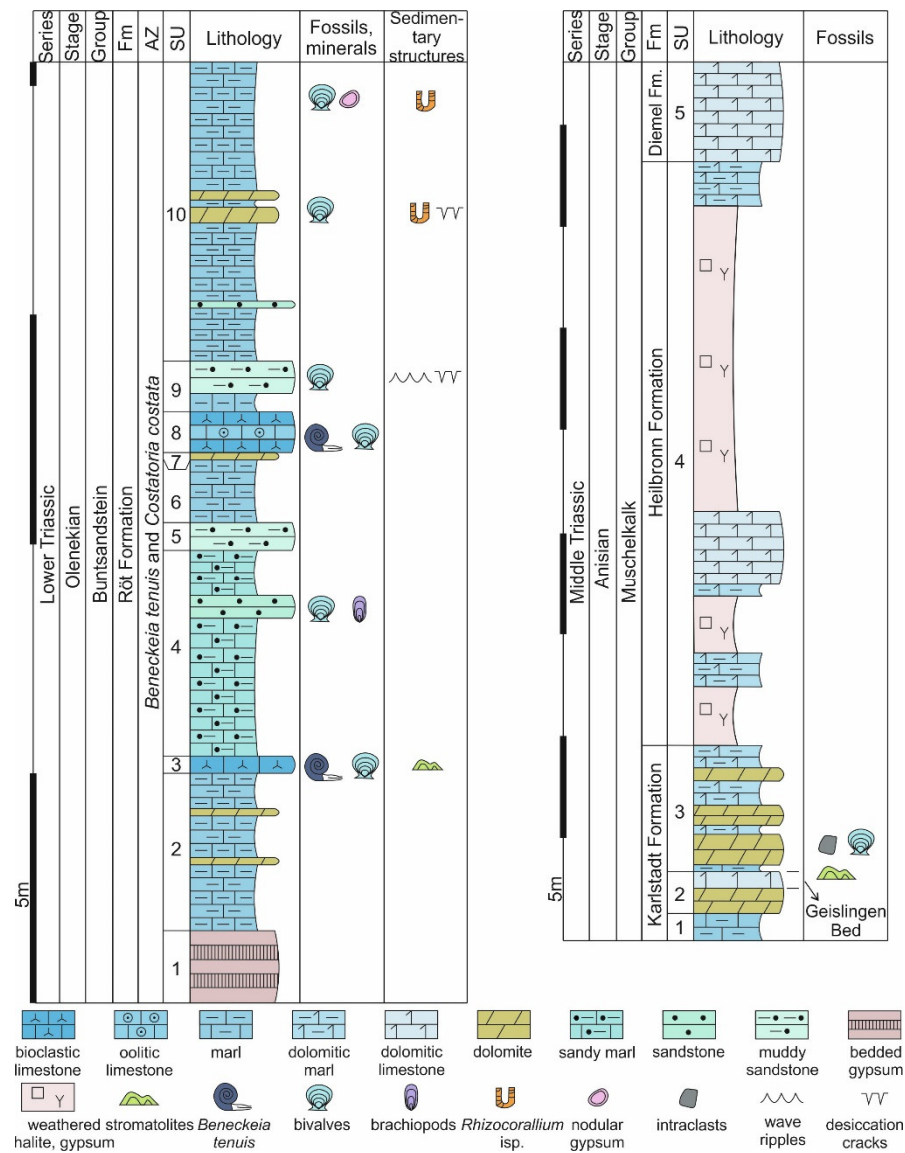


**Figure 2.** Stratigraphy, sedimentology, and palaeontology of sections from the Jena area (Upper Buntsandstein, Olenekian, Lower Triassic, and Germanic Basin; **left**) and Werbach (Lower Middle Muschelkalk, Anisian, Middle Triassic, and Germanic Basin; **right**). Fm = Formation. AZ = Ammonoid Zone. SU = Stratigraphic Unit.

### 3. Materials and Methods

#### 3.1. Fieldwork and Petrography

Sections in the Jena area and at Werbach were examined in the field, and fresh samples were taken (stromatolites from the Jena area, stromatolites and associated facies from Werbach, and microbe-metazoan build-ups from Hardheim). Petrographic thin sections were prepared and analysed using a Zeiss SteREO Discovery.V12 stereomicroscope coupled to an AxioCamMRC camera. The samples were then further studied by means of analytical imaging techniques and stable isotope analyses (see below).

#### 3.2. Analytical Imaging Techniques

Micro-X-ray fluorescence ( $\mu$ -XRF) was applied to obtain element distribution images of the sampled stromatolites and microbe-metazoan build-ups. The analyses were conducted with a Bruker M4 Tornado instrument equipped with an XFlash 430 Silicon Drift Detector.

Measurements (spatial resolution = 25–50  $\mu\text{m}$ , pixel time = 8–25 ms) were performed at 50 kV and 400  $\mu\text{A}$  with a chamber pressure of 20 mbar.

Raman spectroscopy analyses included point measurements (single spectra) and mapping (spectral images). For these analyses, a WITec alpha300R fiber-coupled ultra-high throughput spectrometer was used. Before analysis, the system was calibrated using an integrated light source. The experimental setup included a laser with an excitation wavelength of 532 nm, an automatically controlled laser power of 20 mW, a  $100\times$  long working distance objective with a numerical aperture of 0.75, and a  $300\text{ g mm}^{-1}$  grating. The spectrometer was centered at  $2220\text{ cm}^{-1}$ , covering a spectral range from  $68\text{ cm}^{-1}$  to  $3914\text{ cm}^{-1}$ . This setup had a spectral resolution of  $2.2\text{ cm}^{-1}$ . For single spectra, each spectrum was collected by two accumulations with an integration time of 2 s. For Raman spectral images, spectra were collected at a step size of  $1\text{ }\mu\text{m}$  in the horizontal and vertical direction by an integration time of 0.25 s for each spectrum. Automated cosmic ray correction, background subtraction, and fitting using a Lorentz function were performed using the WITec ProjectFIVE 5.3. Raman images were additionally processed by spectral averaging/smoothing and component analysis.

### 3.3. Stable Isotope Analyses ( $\delta^{13}\text{C}_{\text{carb}}$ , $\delta^{18}\text{O}_{\text{carb}}$ )

Fifteen samples (ca. 100  $\mu\text{g}$  each) of individual mineral phases were obtained from polished rock slabs by using a high-precision drill. The measurements were performed at  $70\text{ }^\circ\text{C}$  using a Thermo Scientific Kiel IV carbonate device coupled to a Finnigan DeltaPlus gas isotope mass spectrometer. Carbon and oxygen stable isotope ratios of carbonate minerals are reported as delta values ( $\delta^{13}\text{C}_{\text{carb}}$  and  $\delta^{18}\text{O}_{\text{carb}}$ , respectively) relative to the Vienna Pee Dee Belemnite (VPDB) reference standard. The standard deviation was 0.08‰ for  $\delta^{13}\text{C}_{\text{carb}}$  and 0.11‰ for  $\delta^{18}\text{O}_{\text{carb}}$ .

All preparation and analytical work were carried out at the Geoscience Center of the Georg-August-Universität Göttingen.

## 4. Results

### 4.1. Stromatolites from the Jena Area (Upper Buntsandstein, Olenekian, Lower Triassic)

The Jena area section begins with a 1.5 m thick stratigraphic unit of bedded gypsum but no fossils (SU 1) (Figure 2). This unit is followed by a  $\sim 3.5$  m thick interval of greyish-green marls with two intercalated dolomite layers (SU 2). The marl interval is overlain by a 0.5 m thick unit of grey bioclastic limestone (*Tenuis*-bank) (SU 3) which is marked by the first occurrence of the ammonoid *Beneckeia tenuis*. In addition to ammonites, the *Tenuis*-bank contains various bivalves such as *Pseudomyoconcha gastrochaena*, *Hoernesia socialis*, *Neoschizodus elongatus*, *Neoschizodus ovatus*, and *Costatoria costata*. It is directly followed by a 10 cm thick stromatolite unit, which can be divided into a lower nonlaminated and an upper laminated part (Figures 2 and 3a). The lamination is planar to wavy (Figure 4a) but locally appears to be disrupted (Figure 4b). The stromatolite unit consists mainly of dolomite as indicated by  $\mu$ -XRF and Raman spectroscopy (Figures 5 and 6). It is overlain by a  $\sim 4.5$  m thick interval of greyish-green sandy marl (SU 4). The upper part of this interval contains a 0.6 m thick bed of greyish-green sandstone that contains fossils of various bivalves (*Pleuromya musculooides*, *Bakevella mytiloides*, and *Costatoria costata*) and brachiopods (*Lingularia tenuissima*).

The top half of the section starts with a  $\sim 0.7$  m thick unit of red muddy sandstone (SU 5), followed by a  $\sim 1.3$  m thick greyish-green marl unit (SU 6) and a  $\sim 0.1$  m thick dolomite unit (SU 7) (Figure 2). The dolomite unit is overlain by a  $\sim 0.9$  m thick interval of bioclastic limestones with abundant fossils (e.g., *Costatoria costata*, *Neoschizodus elongatus*, and *Beneckeia tenuis*) and an oolitic limestone layer (SU 8). The succession continues with a thin marl layer and a  $\sim 0.8$  m thick red muddy sandstone layer that shows wave ripple structures, desiccation cracks, and various types of bivalves (SU 9). The section is terminated by a  $\sim 6.5$  m thick interval of greyish-green marl, intercalated with thin layers of sandstone, and grey dolomite (SU 10). The dolomite layers exhibit wave ripples and contain

body and trace fossils (e.g., *Costatoria costata*, *Rhizocorallium* isp.). The uppermost part of the greyish-green interval contains red gypsum nodules and fossils (bivalves: *Leptochondria albertii*, *Costatoria costata*; trace fossil: *Rhizocorallium* isp.) (Figure 2).

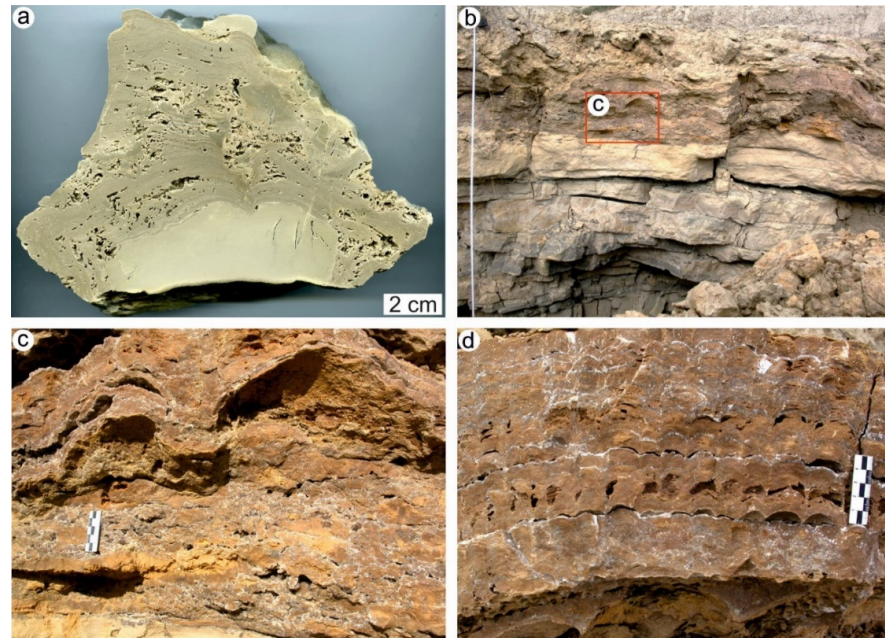


**Figure 3.** Stromatolites from the Jena area (a); polished slab; Röt Formation, SU 3, and Werbach (b–d); outcrop photos; Karlstadt Formation, SU 2. Note that stromatolites from the Jena area can be divided into a lower nonlaminated and an upper laminated part (a), and that stromatolites from the Werbach exhibit columnar shapes (d). The rectangle in (b) is magnified in (c). The scale in (c,d) is 5 cm.

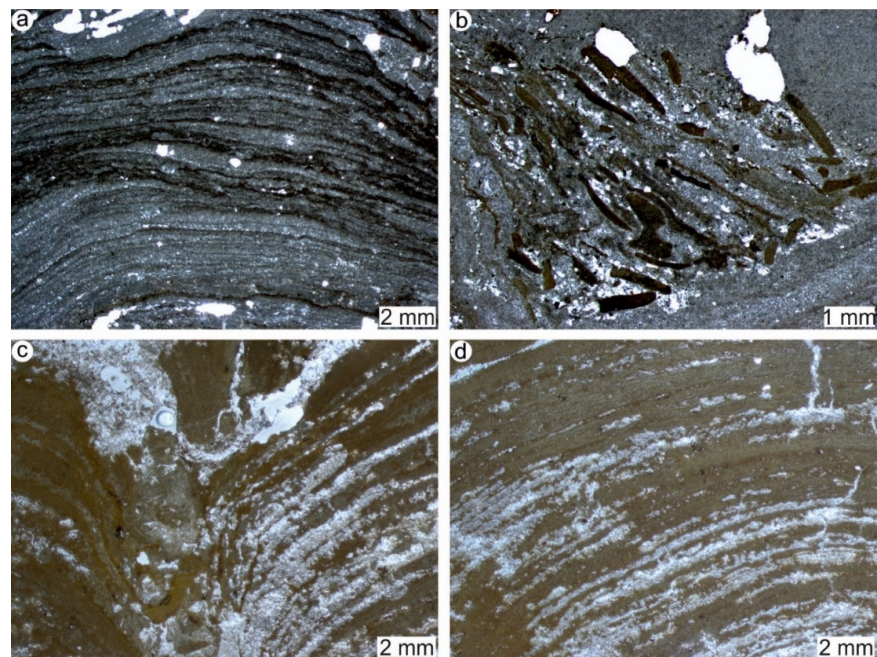


**Figure 4.** Thin section images (transmitted light) of stromatolites from the Jena area (a,b) and Werbach (c,d). Stromatolites from the Jena area exhibit planar to wavy laminations (a) that are locally disrupted, resulting in dislocated intraclasts (b). Stromatolites from Werbach show wavy to columnar laminations (c,d).

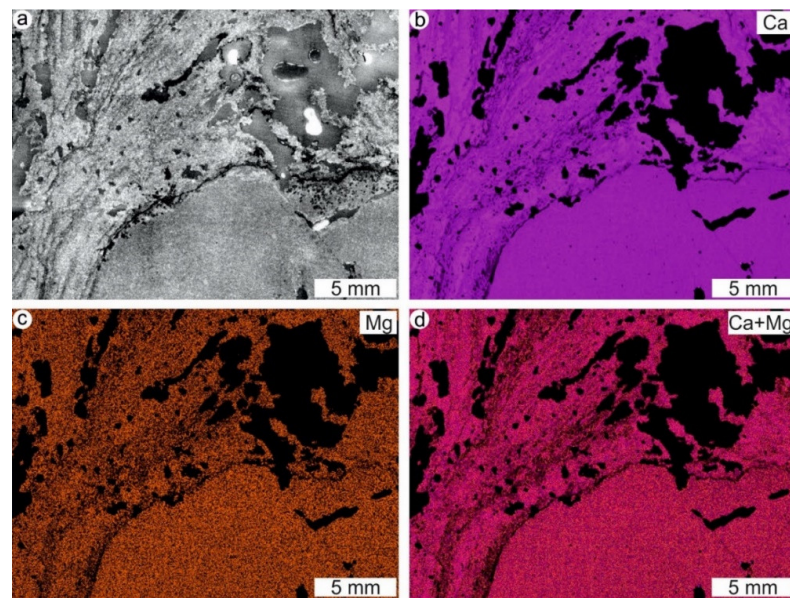


**Figure 5.** Micro X-ray fluorescence ( $\mu$ -XRF) images for a stromatolite from the Jena area. (a) Scan image (reflected light). (b) Calcium (Ca) distribution. (c) Magnesium (Mg) distribution. (d) Calcium (Ca) plus Magnesium (Mg) distribution.

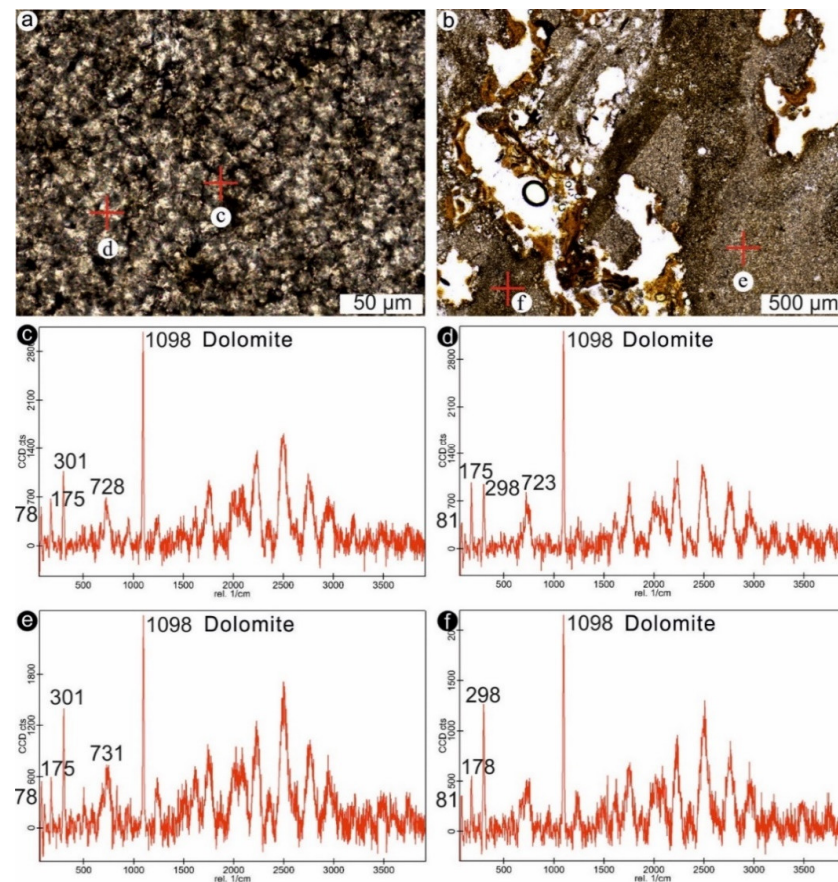


**Figure 6.** Raman spectroscopy data (single spectra) for a stromatolite from the Jena area. (a,c,d) Raman spectra of dolomite in the lower nonlaminated part of the stromatolite. (b,e,f) Raman spectra of dolomite in the upper laminated part of the stromatolite. The unmarked peaks in (c–f) are attributed to fluorescence interference in Raman spectroscopy.

#### 4.2. Stromatolites from Werbach (Middle Muschelkalk, Anisian, Middle Triassic)

In the case of Werbach, our study focused on the Karlstad Formation, which constitutes the lower part of the section. The relevant part begins with a ~1.2 m thick unit of grey marl (SU 1) (Figure 2). This passes into a ~1.2 m thick layer of ochre-coloured dolomite and a ~1 m thick layer of ochre-coloured dolomitic limestone with about 25 cm thick stromatolites (SU 2) (Figures 2 and 3b–d). Unit 2 corresponds to the Geislingen Bed, a supraregional marker horizon [66]. The stromatolites exhibit columnar shapes (Figure 3d) and wavy to columnar laminations (Figure 4c,d). They are mainly composed of calcite as revealed by  $\mu$ -XRF and Raman spectroscopy (Figures 7 and 8) but locally contain dolomite crystals (Figure 8b,e). Following the dolomitic limestone with stromatolites, the section continues with a ~6.5 m thick interval of alternating grey dolomite and dolomitic marl layers (SU 3). Bivalve fossils and intraclasts are observed at the base of this interval. The thickness of the above Heilbronn Formation is strongly reduced due to subsurface dissolution. It mainly consists of halite and gypsum, intercalated with dolomitic marls and limestones (SU 4). The section ends with the Diemel Formation, characterized by dolomitic limestones (SU 5) (Figure 2).

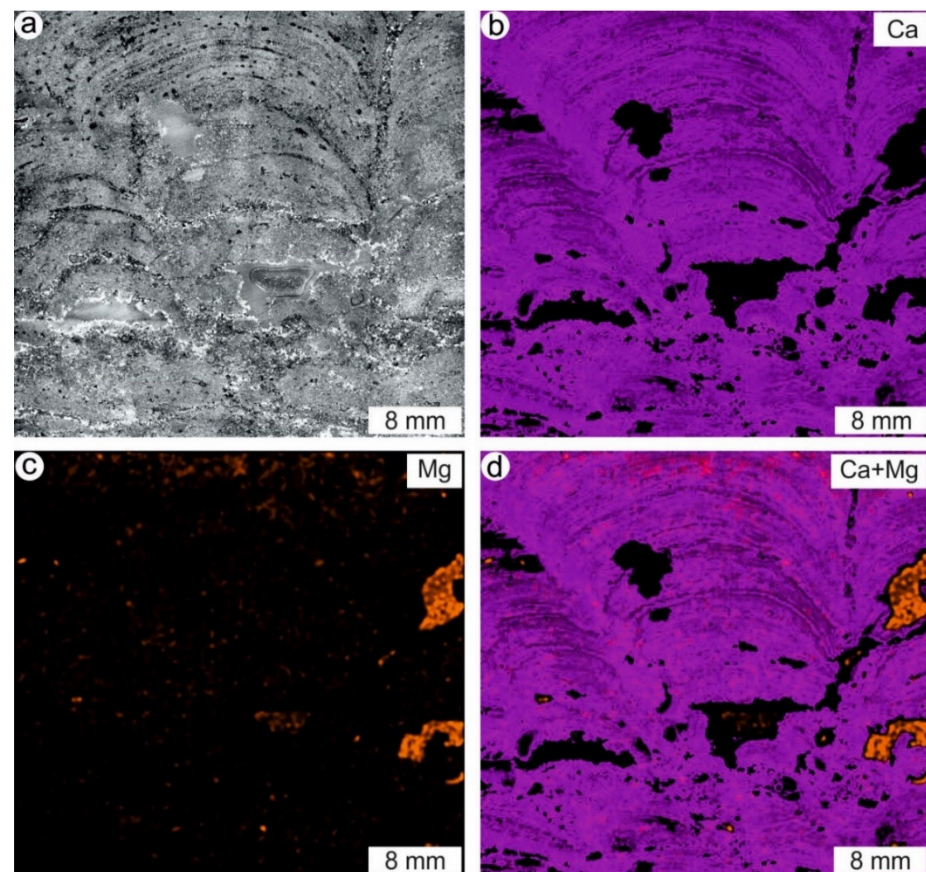


**Figure 7.** Micro X-ray fluorescence ( $\mu$ -XRF) images for a stromatolite from Werbach. (a) Scan image (reflected light). (b) Calcium (Ca) distribution. (c) Magnesium (Mg) distribution. (d) Calcium (Ca) plus Magnesium (Mg) distribution.

#### 4.3. Microbe-Metazoan Build-Ups from Hardheim (Middle Muschelkalk, Anisian, Middle Triassic)

Microbe-metazoan build-ups from Hardheim are ~10 cm thick (Figure 9). The build-ups generally consist of calcite and dolomite but also contain quartz, anatase, and organic matter, as demonstrated by  $\mu$ -XRF and Raman spectroscopy (Figures 10–12). Two types of dolomite can be distinguished, that is, euhedral crystals of pure dolomite (Figure 12c) and anhedral crystals with organic matter (Figure 12d). The microbe-metazoan build-ups



are characterized by distinctly laminated columns (Figure 9). The laminae either consist of pure calcite or of calcite containing organic matter (Figure 11a,c,d). Possible nonspicular (“keratose”) demosponges can be found between and within the columns (Figure 13). The sponges can clearly be distinguished by mesh-like fabrics and clotted to peloidal features [40]. The clotted to peloidal parts are composed of calcite and contain organic matter (Figure 11b,e), whilst areas characterized by mesh-like fabrics solely consist of calcite (Figure 11b,f).

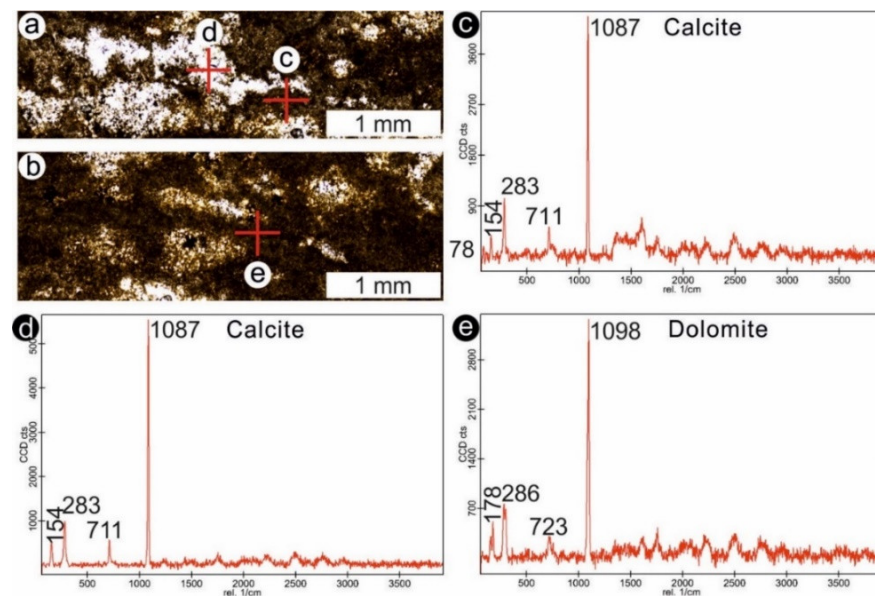


**Figure 8.** Raman spectroscopy data (single spectra) for a stromatolite from Werbach. (a,c,d) Raman spectra of calcite. (b,e) Raman spectra of dolomite. The unmarked peaks in (c–e) are attributed to fluorescence interference in Raman spectroscopy.



**Figure 9.** Overview photo of a microbe-metazoan build-up from Hardheim. The build-up is of a polished slab. It is mainly composed of columnar laminations.

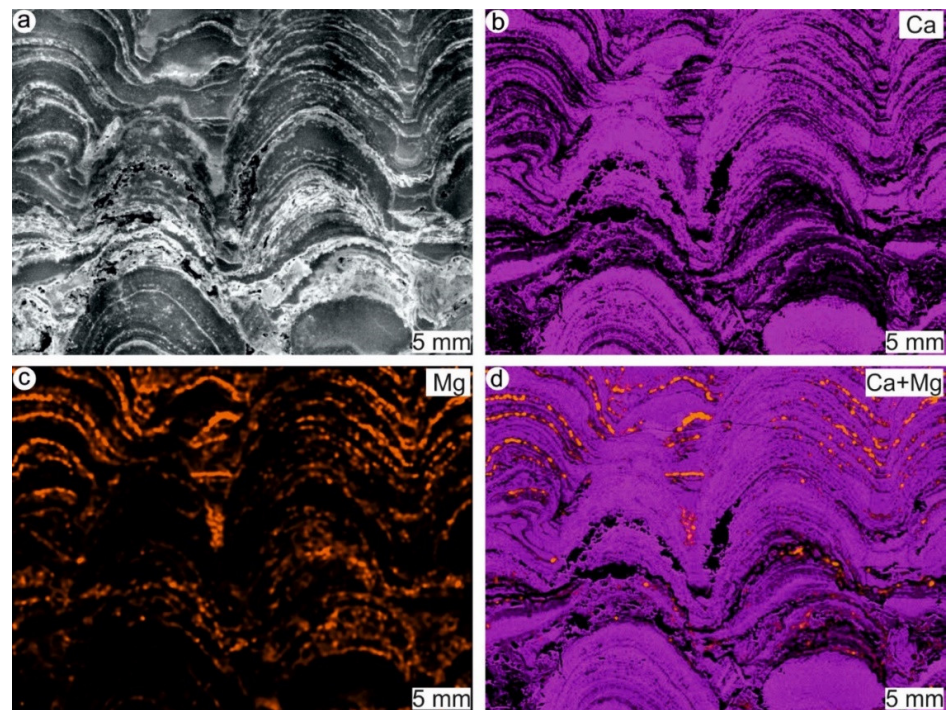


**Figure 10.** Micro X-ray fluorescence ( $\mu$ -XRF) images of a microbe-metazoan build-up from Hardheim. (a) Scan image (reflected light). (b) Calcium (Ca) distribution. (c) Magnesium (Mg) distribution. (d) Calcium (Ca) plus Magnesium (Mg) distribution.

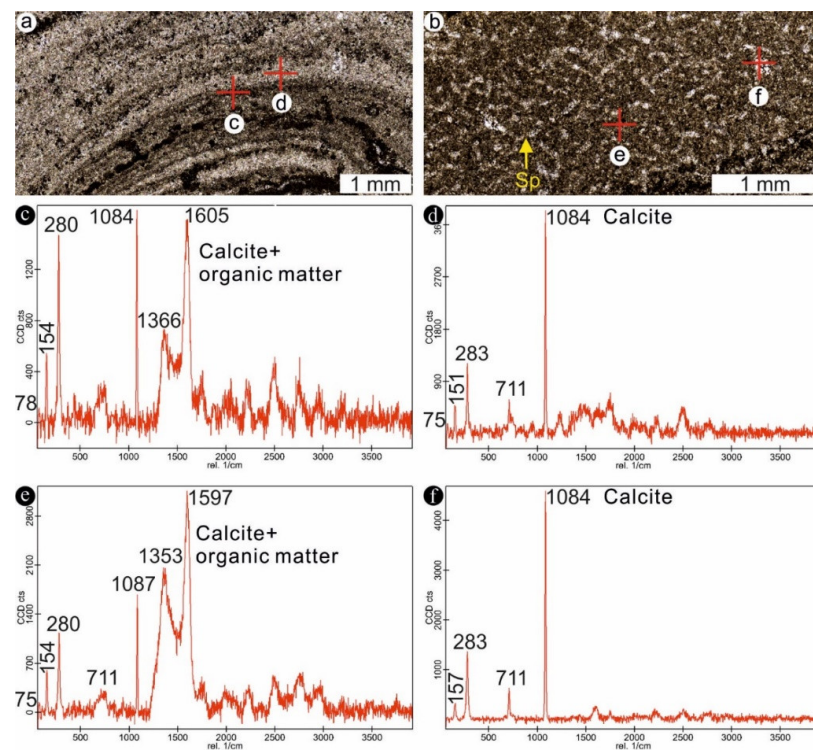


**Figure 11.** Raman spectroscopy data (single spectra) of a microbe-metazoan build-up from Hardheim. (a,c,d) Laminae consist of either calcite containing organic matter or pure calcite (d). (b,e,f) Clotted to peloidal parts of possible nonspicular demosponge fossils (Sp) consist of calcite and contain organic matter (e), while areas characterized by mesh-like fabrics solely consist of calcite (f). The unmarked peaks in (c–f) are attributed to fluorescence interference in Raman spectroscopy.

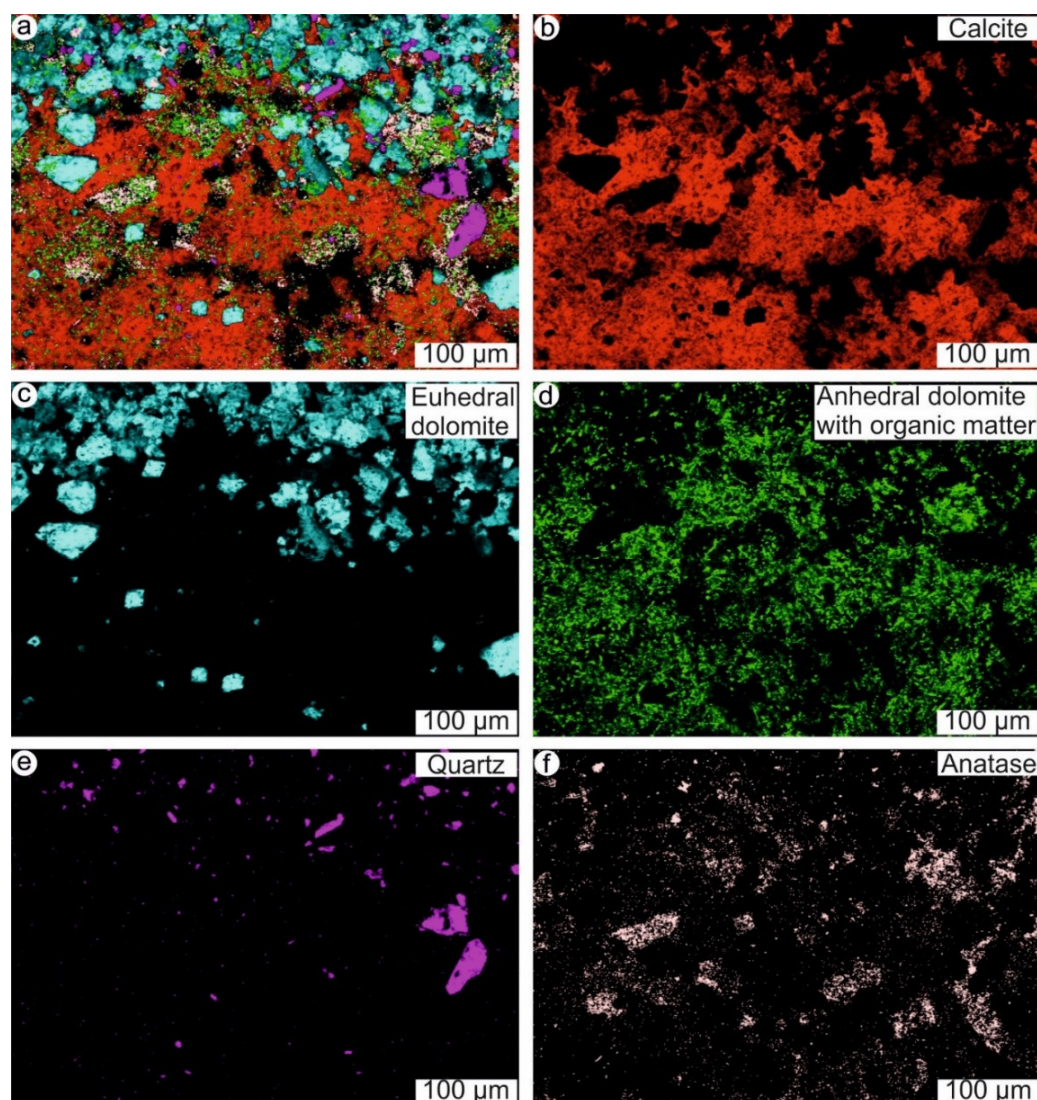


**Figure 12.** Raman spectroscopy data (spectral images) of a microbe-metazoan build-up from Hardheim (location of analytical map is indicated in Figure 13a). (a) Combined image of calcite, dolomite, quartz, anatase, and organic matter. (b) Distribution of calcite. (c) Distribution of pure euohedral dolomite. (d) Distribution of anhedral dolomite with organic matter. (e) Distribution of quartz. (f) Distribution of anatase.

#### 4.4. Carbon and Oxygen Stable Isotopes ( $\delta^{13}\text{C}_{\text{carb}}$ , $\delta^{18}\text{O}_{\text{carb}}$ )

$\delta^{13}\text{C}_{\text{carb}}$  and  $\delta^{18}\text{O}_{\text{carb}}$  data for microbialites from the different localities clustered in three discrete groups (Figure 14; Table 1).  $\delta^{13}\text{C}_{\text{carb}}$  and  $\delta^{18}\text{O}_{\text{carb}}$  values of Group 1 (Jena area stromatolite) ranged from  $-5.5\text{‰}$  to  $-4.7\text{‰}$  and  $-2.1\text{‰}$  to  $-0.6\text{‰}$ , respectively.  $\delta^{13}\text{C}_{\text{carb}}$  values of Group 2 (Werbach stromatolite) varied between  $-5.8\text{‰}$  and  $-5.5\text{‰}$ , in a similar range to those of Group 1.  $\delta^{18}\text{O}_{\text{carb}}$  signatures of these samples, however, appeared to be more negative, with an average value of  $-6.5\text{‰}$ . Marl samples from below the stromatolite layer at Werbach exhibited completely different  $\delta^{13}\text{C}_{\text{carb}}$  and  $\delta^{18}\text{O}_{\text{carb}}$  values, ranging from  $1.3\text{‰}$  to  $1.5\text{‰}$  and  $-2.0\text{‰}$  to  $-1.9\text{‰}$ , respectively.  $\delta^{13}\text{C}_{\text{carb}}$  and  $\delta^{18}\text{O}_{\text{carb}}$  values of Group 3 (Hardheim microbe-metazoan build-up) varied from  $-1.5\text{‰}$  to  $0.6\text{‰}$  and  $-6.8\text{‰}$  to  $-5.8\text{‰}$ , respectively. An extraclast contained in a microbe-metazoan build-up from Hardheim had a  $\delta^{13}\text{C}_{\text{carb}}$  value of  $-4.7\text{‰}$  and a  $\delta^{18}\text{O}_{\text{carb}}$  value of  $-6.6\text{‰}$  (Figure 14; Table 1).

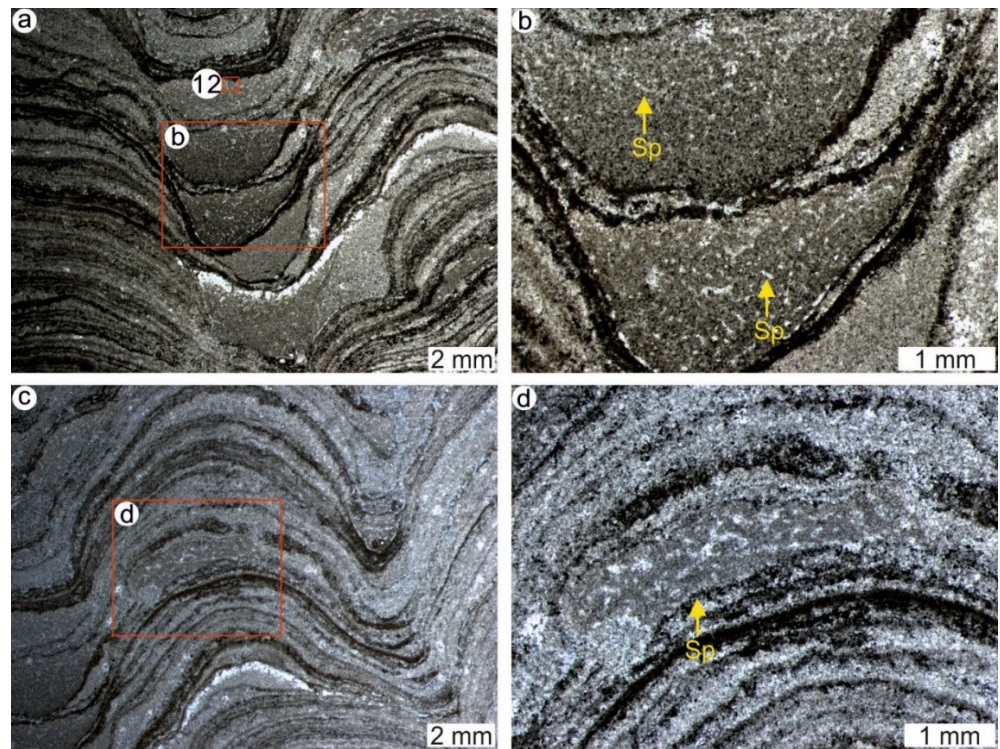


**Figure 13.** Thin section images (transmitted light) of a microbe-metazoan build-up from Hardheim. (a,b) Possible nonspicular demosponges (Sp) between the laminated columns, showing characteristic mesh-like fabrics and clotted to peloidal features (red box in (a) enlarged in (b)). (c,d) Possible nonspicular demosponges within laminated columns (red box in (c) enlarged in (d)).

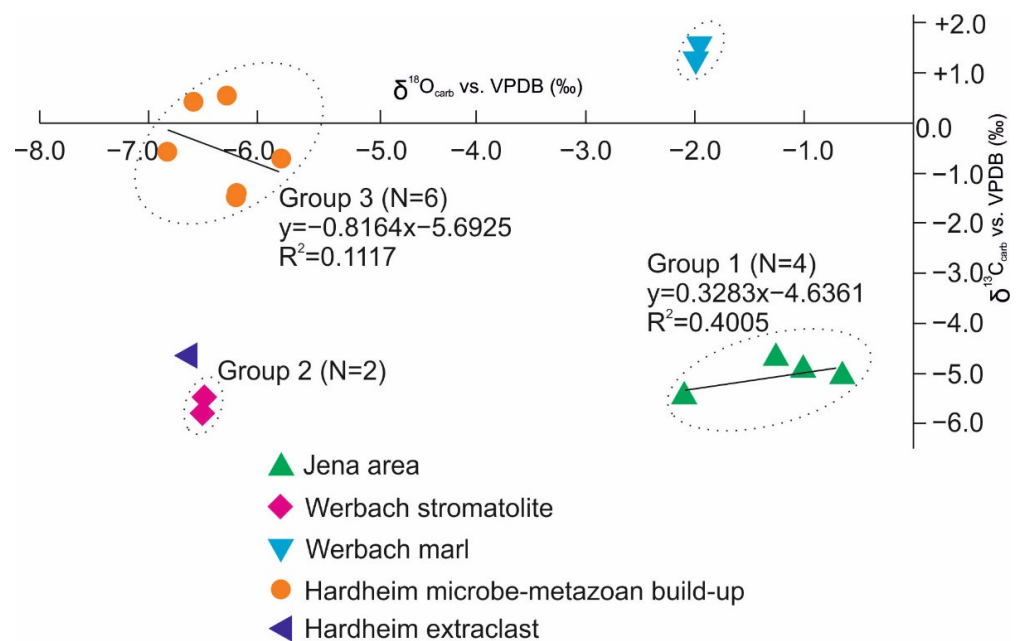


**Figure 14.** Carbon and oxygen stable isotope data ( $\delta^{13}\text{C}_{\text{carb}}$  and  $\delta^{18}\text{O}_{\text{carb}}$ , respectively) for microbialites from the Jena area, Werbach, and Hardheim.

**Table 1.** Carbon and oxygen stable isotope data ( $\delta^{13}\text{C}_{\text{carb}}$  and  $\delta^{18}\text{O}_{\text{carb}}$ , respectively) for microbialites from the Jena area, Werbach, and Hardheim.

Sample Name	Sample Number	$\delta^{13}\text{C}_{\text{carb}}$ vs. VPDB (‰)	$\delta^{18}\text{O}_{\text{carb}}$ vs. VPDB (‰)
Jena area stromatolite	4	−4.7	−1.3
		−4.9	−1.0
		−5.5	−2.1
		−5.1	−0.6
Werbach stromatolite	2	−5.8	−6.5
		−5.5	−6.5
Werbach marl	2	1.3	−2.0
		1.5	−1.9
Hardheim microbe-metazoan build-up	6	−0.6	−6.8
		−0.7	−5.8
		−1.4	−6.2
		−1.5	−6.2
		0.4	−6.6
		0.6	−6.3
Hardheim extraclast	1	−4.7	−6.6

$\delta^{13}\text{C}_{\text{carb}}$  and  $\delta^{18}\text{O}_{\text{carb}}$  values of Group 1 (Jena area stromatolite) showed a relatively low coefficient of determination ( $R^2 = 0.4005$ ;  $n = 4$ ) (Figure 14), which might indicate a small effect of diagenetic alteration [67]. The  $R^2$  value for Group 3 (Hardheim microbe-metazoan build-up) was also low (0.1117;  $n = 6$ ) and may be interpreted similarly (Figure 14). However, the significantly negative  $\delta^{18}\text{O}_{\text{carb}}$  values of Group 3 perhaps reflect meteoric influence during diagenesis [68], which could also be the case for Group 2 (Werbach stromatolite).

## 5. Discussion

### 5.1. Sedimentary Environments

During Permian and Triassic times, the Germanic Basin was located on the edge of the subtropical Tethys Ocean systems [62–64] (Figure 1). In the Olenekian, a transgression from the Tethys via the East Carpathian Gate resulted in the establishment of marine shelf environments in the surroundings of South Poland. Temporary, short-term transgressions entered the central Germanic basin. In the area of Thuringia, this is reflected by the widespread deposition of marls, limestones, and dolomites, together with oolitic limestones and stromatolites. Changes in sea level and/or clastic input resulted in the subsequent deposition of marls and siliciclastic sediments. Desiccation cracks and gypsum nodules at the base and top of the section suggest slightly evaporitic conditions during deposition.

Strata of the Werbach section belong to the Middle Muschelkalk Subgroup (Anisian, Middle Triassic) and are thus stratigraphically younger than those exposed in the Jena area (Figure 2). Lithologically, the Werbach section comprises evaporites and carbonates such as dolomites, limestones, and marls [66] (Figure 2). The lack of fossils except for local occurrences of fauna that could cope with elevated salinities [66] suggest saline lagoonal environments. Since Hardheim is palaeogeographically proximal to Werbach (Figure 1), and the microbialites at both sections can be correlated stratigraphically [66], a similar palaeoenvironment appears plausible.  $\delta^{13}\text{C}_{\text{carb}}$  values indicate that microbe-metazoan build-up at Hardheim thrived under marine conditions, while the habitats of stromatolites from the Jena area might have been influenced by freshwater. This is in good accordance with palaeogeographic reconstructions, suggesting an increased connection between the

Germanic Basin and the Tethys Ocean during the Lower-Middle Triassic [63,65] (Figure 1). Nonetheless, combined sedimentological and palaeontological evidence indicate that the investigated stromatolites/microbe-metazoan build-ups probably formed in slightly evaporitic environments, which might prevailed in certain areas.

### 5.2. Stromatolites vs. Microbe-Metazoan Build-Ups

Olenekian stromatolites from the Jena area exhibited planar to wavy laminations (Figure 4a) and consisted mainly of dolomite (Figures 5 and 6). Anisian stromatolites from Werbach showed wavy to columnar laminations (Figure 4c,d) but were mainly composed of calcite (Figures 7 and 8), which perhaps formed through dedolomitization [69]. Microbe-metazoan build-ups at Hardheim were characterized by columnar laminations (Figure 9) and consisted mainly of calcite, dolomite, and organic matter (Figures 10–12). The distinct lamination textures resulted from the relative proportion of organic matter (Figure 11a,c,d). Organic matter in some of the laminae likely indicates that mineral formation was associated with exopolymeric substances (EPS) secreted by microbial mat communities [70–72], although trapping and binding of detrital materials might also have played a role in some cases [73].

The major difference between all the studied microbialites was the presence of possible nonspicular demosponges in microbe-metazoan build-ups from Hardheim. As discussed above, nonspicular demosponges occur between and within laminated columns and are readily discernible by mesh-like fabrics and clotted to peloidal features (Figure 13). Such textures have already been described in the aftermath of the Permian–Triassic crisis from the western USA [46,74,75], South China [76], Iran [16,49], southern Armenia [48], and the Germanic Basin [40]. Similar occurrences were also reported from the early Palaeozoic [50,51] and the early Neoproterozoic [52].

Enigmatic mesh-like fabrics and clotted to peloidal features were previously interpreted as filamentous cyanobacteria [25], green algae [77], or hexactinellid sponges [61]. However, three-dimensional reconstructions of modern nonspicular demosponges revealed the presence of mesh-like fabrics and clotted to peloidal features that are much more similar to characteristics observed in some ancient records. In such cases, mesh-like fabrics in fossil record represent skeletal elements of nonspicular demosponges originally consisting of spongin/chitin [38–40] (Figure 1). The clotted to peloidal features, in contrast, reflect automicrite that form through the in situ microbial decay of microbe-rich sponge tissue [78,79].

Anhedral dolomite crystals in microbial-metazoan build-ups from Hardheim contained organic matter (Figure 12d). They were tentatively attributed to protodolomite (cf. [80]), which hypothetically may be related to microbial sulfate reduction [81,82]. Various modern demosponges (e.g., *Chondrosia reniformis*, *Petrosia ficiformis* and *Geodia barretti*) harbour abundant sulfate-reducing bacteria. Notably, taphonomically mineralized tissue of these sponges contained pyrite crystals, which is a typical end product of microbial sulfate reduction [83–86]. It is, thus, tempting to speculate that the anhedral dolomite crystals in microbe-metazoan build-ups from Hardheim resulted from taphonomic processes associated with the sponges.

### 5.3. Palaeoecological Implications of the Microbialites

The Permian–Triassic crisis was characterized by a potentially catastrophic decline in biodiversity in marine and terrestrial ecosystems [87–90]. Furthermore, it was associated with ubiquitous occurrences of unusual sedimentary features, including microbialites (e.g., [9–19]). As stated before, microbe-metazoan build-ups containing nonspicular demosponges are easily overlooked in geological records but have received increasing attention recently [16,38–40,46–52,74,75]. One possible explanation for the widespread occurrence of diverse microbial mats is a suppressed ecological competition with grazing metazoans that would prevent their development [20]. Although the details remain to be studied, it is plausible that microbes and nonspicular demosponges had a mutualistic relationship [39,50],

which allowed them to thrive under ecologically restrictive conditions [40]. Given the possible presence of nonspicular demosponges in early Neoproterozoic environments [52], it is tempting to speculate that microbial-metazoan build-ups reflect an ancient evolutionary and ecologic association that date back to the origin of animal life.

The Lower-Middle Triassic microbialites and microbe-metazoan build-ups studied herein formed in slightly evaporitic environments. The presented study, thus, lends further support to the idea that the development of such communities was influenced by water depth and salinity [39,40]. Indeed, the distribution of stromatolites and/or microbe-metazoan build-ups might have been controlled by subtle differences in salinity and water depth, the latter influencing hydrodynamic processes and nutrient supply down to the microscale. This may explain the preferential development of nonspicular sponges in morphological valleys between laminated columns, since these areas might have been characterized by slightly different conditions as compared to the top parts of the columns.

## 6. Conclusions

Triassic microbialites from the Jena area (Upper Buntsandstein Subgroup, Olenekian, and Lower Triassic) as well as from Werbach and Hardheim (both lower Middle Muschelkalk Subgroup, Anisian, Middle Triassic) formed in slightly evaporitic environments. Olenekian stromatolites in the Jena area exhibited planar to wavy laminations, while Anisian stromatolites from Werbach were characterized by wavy to columnar laminations. Anisian microbe-metazoan build-ups from Hardheim consisted of columnar laminations. The presence of nonspicular demosponges that originally consisted of spongin/chitin supports that these organisms can be preserved in geological time. The taphonomic key process was organomineralization linked to the microbial degradation of sponge tissue, ultimately resulting in the formation of characteristic clotted to peloidal features. The proliferation of microbial mats and/or microbe-metazoan build-ups was likely due to the suppressed ecological competition after the Permian–Triassic crisis. It is plausible that microbes and nonspicular demosponges in the build-ups had a mutualistic relationship, and it is tempting to speculate that this association reflects an ancient evolutionary and ecologic strategy. Given the palaeoenvironments, water depth and salinity might have been the most important ecological controls on the presence of nonspicular demosponges.

**Author Contributions:** Conceptualization, Y.P. and J.R.; methodology, Y.P.; software, Y.P.; formal analysis, Y.P. and J.R.; resources, H.H. and T.V.; data curation, Y.P.; writing—original draft preparation, Y.P.; writing—review and editing, Y.P., J.R., H.H., T.V. and J.-P.D.; supervision, J.R.; funding acquisition, Y.P. All authors have read and agreed to the published version of the manuscript.

**Funding:** This study was financially supported by the China Scholarship Council.

**Data Availability Statement:** Not applicable.

**Acknowledgments:** We thank Brian Richard Pratt and two other anonymous reviewers for valuable comments. Axel Hackmann, Burkhard Schmidt, Dennis Kohl, Jan Schöning and Thierry Wasselin are thanked for lab assistance. Thomas Billert is thanked for providing stromatolites from the Jena area.

**Conflicts of Interest:** The authors declare that they have no competing interests. All authors have approved this manuscript and no author has financial or other contractual agreements that might cause conflicts of interest.

## References

1. Burne, R.V.; Moore, L.S. Microbialites: Organosedimentary deposits of benthic microbial communities. *Palaios* **1987**, *2*, 241–254. [[CrossRef](#)]
2. Arp, G.; Reimer, A.; Reitner, J. Photosynthesis-induced biofilm calcification and calcium concentrations in Phanerozoic oceans. *Science* **2001**, *292*, 1701–1704. [[CrossRef](#)] [[PubMed](#)]
3. Riding, R.; Liang, L. Geobiology of microbial carbonates: Metazoan and seawater saturation state influences on secular trends during the Phanerozoic. *Palaeogeogr. Palaeoclim. Palaeoecol.* **2005**, *219*, 101–115. [[CrossRef](#)]
4. Riding, R. Microbial carbonate abundance compared with fluctuations in metazoan diversity over geological time. *Sediment. Geol.* **2006**, *185*, 229–238. [[CrossRef](#)]

5. Walter, M.R.; Buick, R.; Dunlop, J.S.R. Stromatolites 3400–3500 Myr old from the North Pole area, Western Australia. *Nature* **1980**, *284*, 443–445. [[CrossRef](#)]
6. Riding, R. The nature of stromatolites: 3500 million years of history and a century of research. In *Advances in Stromatolite Geobiology*; Reitner, J., Quéric, N.V., Arp, G., Eds.; Springer: Berlin/Heidelberg, Germany, 2011; pp. 29–74.
7. Duda, J.-P.; Van Kranendonk, M.J.; Thiel, V.; Ionescu, D.; Strauss, H.; Schäfer, N.; Reitner, J. A Rare glimpse of Paleo-archean life: Geobiology of an exceptionally preserved microbial mat facies from the 3.4 Ga Strelley Pool Formation, Western Australia. *PLoS ONE* **2016**, *11*, e0147629. [[CrossRef](#)]
8. Pratt, B.R. Stromatolite decline—A reconsideration. *Geology* **1982**, *10*, 512–515. [[CrossRef](#)]
9. Kershaw, S.; Zhang, T.; Lan, G. A microbialite crust at the Permian–Triassic boundary in South China, and its palaeoenvironmental significance. *Palaeogeogr. Palaeoclimatol. Palaeoecol.* **1999**, *146*, 1–18. [[CrossRef](#)]
10. Kershaw, S.; Crasquin, S.; Li, Y.; Collin, P.-Y.; Forel, M.-B.; Mu, X.; Baud, A.; Wang, Y.; Xie, S.; Maurer, F.; et al. Microbialites and global environmental change across the Permian–Triassic boundary: A synthesis. *Geobiology* **2012**, *10*, 25–47. [[CrossRef](#)]
11. Kershaw, S.; Tang, H.; Li, Y.; Guo, L. Oxygenation in carbonate microbialites and associated facies after the end-Permian mass extinction: Problems and potential solutions. *J. Palaeogeogr.* **2018**, *7*, 32–47. [[CrossRef](#)]
12. Lehrmann, D.J. Early Triassic calcimicrobial mounds and biostromes of the Nanpanjiang basin, south China. *Geology* **1999**, *27*, 359–362. [[CrossRef](#)]
13. Woods, A.D. Assessing Early Triassic paleoceanographic conditions via unusual sedimentary fabrics and features. *Earth Sci. Rev.* **2014**, *137*, 6–18. [[CrossRef](#)]
14. Wu, Y.S.; Yu, G.L.; Li, R.H.; Song, L.R.; Jiang, H.X.; Riding, R.; Liu, L.J.; Liu, N.Y.; Zhao, R. Cyanobacterial fossils from 252 Ma old microbialites and their environmental significance. *Sci. Rep.* **2014**, *4*, 3820. [[CrossRef](#)] [[PubMed](#)]
15. Wu, S.; Chen, Z.-Q.; Fang, Y.; Pei, Y.; Yang, H.; Ogg, J. A Permian–Triassic boundary microbialite deposit from the eastern Yangtze Platform (Jiangxi Province, South China): Geobiologic features, ecosystem composition and redox conditions. *Palaeogeogr. Palaeoclim. Palaeoecol.* **2017**, *486*, 58–73. [[CrossRef](#)]
16. Heindel, K.; Foster, W.J.; Richoz, S.; Birgel, D.; Roden, V.J.; Baud, A.; Brandner, R.; Krystyn, L.; Mohtat, T.; Koşun, E.; et al. The formation of microbial-metazoan bioherms and biostromes following the latest Permian mass extinction. *Gondwana Res.* **2018**, *61*, 187–202. [[CrossRef](#)]
17. Chen, Z.-Q.; Tu, C.; Pei, Y.; Ogg, J.; Fang, Y.; Wu, S.; Feng, X.; Huang, Y.; Guo, Z.; Yang, H. Biosedimentological features of major microbe-metazoan transitions (MMTs) from Precambrian to Cenozoic. *Earth Sci. Rev.* **2019**, *189*, 21–50. [[CrossRef](#)]
18. Pei, Y.; Chen, Z.-Q.; Fang, Y.; Kershaw, S.; Wu, S.; Luo, M. Volcanism, redox conditions, and microbialite growth linked with the end-Permian mass extinction: Evidence from the Xiajiacao section (western Hubei Province), South China. *Palaeogeogr. Palaeoclim. Palaeoecol.* **2019**, *519*, 194–208. [[CrossRef](#)]
19. Zhang, X.-Y.; Li, Y.; Wang, G.; Yang, H.-Q. Different accretion and diagenetic patterns within the fabrics of the Permian–Triassic boundary microbialites on the Leye isolated carbonate platform, South China Block. *J. Palaeogeogr.* **2021**, *10*, 1–12. [[CrossRef](#)]
20. Foster, W.J.; Heindel, K.; Richoz, S.; Gliwa, J.; Lehrmann, D.J.; Baud, A.; Kolar-Jurkovšek, T.; Aljinović, D.; Jurkovšek, B.; Korn, D.; et al. Suppressed competitive exclusion enabled the proliferation of Permian/Triassic boundary microbialites. *Depos. Rec.* **2020**, *6*, 62–74. [[CrossRef](#)] [[PubMed](#)]
21. Kalkowsky, E. Oolith and Stromatolith im norddeutschen Buntsandstein. *Z. Dtsch. Geol. Ges.* **1908**, *60*, 68–125.
22. Aitken, J.D. Middle Cambrian to Middle Ordovician cyclic sedimentation, southern Rocky Mountains of Alberta. *Bull. Can. Pet. Geol.* **1966**, *14*, 405–441.
23. Riding, R. (Ed.) *Classification of microbial carbonates*. In *Calcareous Algae and Stromatolites*; Springer: Berlin/Heidelberg, Germany, 1991; pp. 21–51.
24. Braga, J.; Martín, J.; Riding, R. Controls on Microbial Dome Fabric Development along a Carbonate-Siliciclastic Shelf-Basin Transect, Miocene, SE Spain. *Palaios* **1995**, *10*, 347. [[CrossRef](#)]
25. Walter, M.R. Stromatolites and the biostratigraphy of the Australian Precambrian and Cambrian. *Spec. Pap. Palaeontol.* **1972**, *11*, 1–256.
26. Dravis, J.J. Hardened Subtidal Stromatolites, Bahamas. *Science* **1983**, *219*, 385–386. [[CrossRef](#)] [[PubMed](#)]
27. Arp, G.; Thiel, V.; Reimer, A.; Michaelis, W.; Reitner, J. Biofilm exopolymers control microbialite formation at thermal springs discharging into the alkaline Pyramid Lake, Nevada, USA. *Sediment. Geol.* **1999**, *126*, 159–176. [[CrossRef](#)]
28. Bosak, T.; Liang, B.; Wu, T.-D.; Templer, S.P.; Evans, A.; Vali, H.; Guerquin-Kern, J.-L.; Klepac-Ceraj, V.; Sim, M.S.; Mui, J. Cyanobacterial diversity and activity in modern conical microbialites. *Geobiology* **2012**, *10*, 384–401. [[CrossRef](#)] [[PubMed](#)]
29. Playford, P.; Cockbain, A.; Druce, E.; Wray, J. Chapter 10.4: Devonian Stromatolites from the Canning Basin, Western Australia. *Dev. Sedimentol.* **1976**, *20*, 543–563.
30. Böhm, F.; Brachert, T.C. Deep-water stromatolites and, Frutexitas Maslov from the early and Middle Jurassic of S-Germany and Austria. *Facies* **1993**, *28*, 145–168. [[CrossRef](#)]
31. Heim, C.; Simon, K.; Ionescu, D.; Reimer, A.; De Beer, D.; Quéric, N.-V.; Reitner, J.; Thiel, V. Assessing the utility of trace and rare earth elements as biosignatures in microbial iron oxyhydroxides. *Front. Earth Sci.* **2015**, *3*, 1–15. [[CrossRef](#)]
32. Heim, C.; Quéric, N.-V.; Ionescu, D.; Schäfer, N.; Reitner, J. Frutexitas-like structures formed by iron oxidizing biofilms in the continental subsurface (Åspö Hard Rock Laboratory, Sweden). *PLoS ONE* **2017**, *12*, e0177542. [[CrossRef](#)] [[PubMed](#)]



33. Mißbach, H.; Duda, J.-P.; van den Kerkhof, A.M.; Lüders, V.; Pack, A.; Reitner, J.; Thiel, V. Ingredients for microbial life preserved in 3.5 billion-year-old fluid inclusions. *Nat. Commun.* **2021**, *12*, 1101. [[CrossRef](#)]
34. Reitner, J.; Peckmann, J.; Blumenberg, M.; Michaelis, W.; Reimer, A.; Thiel, V. Concretionary methane-seep carbonates and associated microbial communities in Black Sea sediments. *Palaeogeogr. Palaeoclim. Palaeoecol.* **2005**, *227*, 18–30. [[CrossRef](#)]
35. Reitner, J.; Peckmann, J.; Reimer, A.; Schumann, G.; Thiel, V. Methane-derived carbonate build-ups and associated microbial communities at cold seeps on the lower Crimean shelf (Black Sea). *Facies* **2005**, *51*, 66–79. [[CrossRef](#)]
36. Arp, G.; Ostertag-Henning, C.; Yücekent, S.; Reitner, J.; Thiel, V. Methane-related microbial gypsum calcitization in stromatolites of a marine evaporative setting (Münder Formation, Upper Jurassic, Hils Syncline, north Germany). *Sedimentology* **2008**, *55*, 1227–1251. [[CrossRef](#)]
37. Reitner, J. Architecture of archaeal-dominated microbial mats from cold seeps in the Black Sea (Dnjepr Canyon, Lower Crimean Shelf). In *Microbial Mats: Modern and Ancient Microorganisms in Stratified Systems, Cellular Origin, Life in Extreme Habitats and Astrobiology*; Seckbach, J., Oren, A., Eds.; Springer: Dordrecht, The Netherlands, 2010; Volume 14, pp. 207–220.
38. Luo, C.; Reitner, J. First report of fossil “keratose” demosponges in Phanerozoic carbonates: Preservation and 3-D reconstruction. *Naturwissenschaften* **2014**, *101*, 467–477. [[CrossRef](#)] [[PubMed](#)]
39. Luo, C.; Reitner, J. ‘Stromatolites’ built by sponges and microbes—A new type of Phanerozoic bioconstruction. *Lethaia* **2016**, *49*, 555–570. [[CrossRef](#)]
40. Pei, Y.; Duda, J.; Schöning, J.; Luo, C.; Reitner, J. Late Anisian microbe-metazoan build-ups in the Germanic Basin: Aftermath of the Permian–Triassic crisis. *Lethaia* **2021**, *54*, 823–844. [[CrossRef](#)]
41. Reitner, J.; Hühne, C.; Thiel, V. Porifera-rich mud mounds and microbialites as indicators of environmental changes within the Devonian/Lower Carboniferous critical interval. *Terra Nostra* **2001**, *4*, 60–65.
42. Rodríguez-Martínez, M.; Sánchez, F.; Walliser, E.O.; Reitner, J. An Upper Turonian fine-grained shallow marine stromatolite bed from the Muñecas Formation, Northern Iberian Ranges, Spain. *Sediment. Geol.* **2012**, *263–264*, 96–108. [[CrossRef](#)]
43. Szulc, J. Middle Triassic (Muschelkalk) sponge-microbial stromatolites, diplopores and Girvanella-oncoids from the Silesian Cracow Upland. In Proceedings of the 3rd IFAA Regional Symposium and IGCP 380 International Meeting, Kraków, Poland, 14–20 September 1997; pp. 10–15.
44. Brayard, A.; Vennin, E.; Olivier, N.; Bylund, K.G.; Jenks, J.F.; Stephen, D.A.; Bucher, H.; Hofmann, R.; Goudemand, N.; Escarguel, G. Transient metazoan reefs in the aftermath of the end-Permian mass extinction. *Nat. Geosci.* **2011**, *4*, 693–697. [[CrossRef](#)]
45. Marengo, P.J.; Griffin, J.M.; Fraiser, M.L.; Clapham, M.E. Paleocology and geochemistry of Early Triassic (Spathian) microbial mounds and implications for anoxia following the end-Permian mass extinction. *Geology* **2012**, *40*, 715–718. [[CrossRef](#)]
46. Vennin, E.; Olivier, N.; Brayard, A.; Bour, I.; Thomazo, C.; Escarguel, G.; Fara, E.; Bylund, K.G.; Jenks, J.F.; Stephen, D.A.; et al. Microbial deposits in the aftermath of the end-Permian mass extinction: A diverging case from the Mineral Mountains (Utah, USA). *Sedimentology* **2015**, *62*, 753–792. [[CrossRef](#)]
47. Luo, C. “Keratose” Sponge Fossils and Microbialites: A Geobiological Contribution to the Understanding of Metazoan Origin. Ph.D. Thesis, Georg-August-Universität Göttingen, Göttingen, Germany, 2015.
48. Friesenbichler, E.; Richoz, S.; Baud, A.; Krystyn, L.; Sahakyan, L.; Vardanyan, S.; Peckmann, J.; Reitner, J.; Heindel, K. Sponge-microbial build-ups from the lowermost Triassic Chanakhchi section in southern Armenia: Microfacies and stable carbon isotopes. *Palaeogeogr. Palaeoclim. Palaeoecol.* **2018**, *490*, 653–672. [[CrossRef](#)]
49. Baud, A.; Richoz, S.; Brandner, R.; Krystyn, L.; Heindel, K.; Mohtat, T.; Mohtat-Aghai, P.; Horacek, M. Sponge Takeover from End-Permian Mass Extinction to Early Induan Time: Records in Central Iran Microbial Buildups. *Front. Earth Sci.* **2021**, *9*, 586210. [[CrossRef](#)]
50. Lee, J.-H.; Riding, R. The ‘classic stromatolite’ Cryptozoön is a keratose sponge-microbial consortium. *Geobiology* **2021**, *19*, 189–198. [[CrossRef](#)] [[PubMed](#)]
51. Pham, D.; Hong, J.; Lee, J.-H. Keratose sponge–microbial consortia in stromatolite-like columns and thrombolite-like mounds of the Lower Ordovician (Tremadocian) Mungok Formation, Yeongwol, Korea. *Palaeogeogr. Palaeoclim. Palaeoecol.* **2021**, *572*, 110409. [[CrossRef](#)]
52. Turner, E.C. Possible poriferan body fossils in early Neoproterozoic microbial reefs. *Nature* **2021**, *596*, 87–91. [[CrossRef](#)]
53. Paul, J.; Peryt, T.M.; Burne, R.V. Kalkowsky’s stromatolites and oolites (Lower Buntsandstein, Northern Germany). In *Advances in Stromatolite Geobiology*; Reitner, J., Quéric, N.-V., Arp, G., Eds.; Springer: Berlin/Heidelberg, Germany, 2011; pp. 13–28.
54. Naumann, E. *Erläuterungen zur Geologischen Karte von Preußen und Benachbarten Deutschen Ländern: Blatt Jena, Gradabteilung 71, Blatt 2, 65 S*; Preußische Geologische Landesanstalt: Berlin, Germany, 1928.
55. Genser, C. *Zur Stratigraphie und Chemie des Mittleren Muschelkalks in Franken: Geologisch und Paläontologische Abhandlungen, Neue Folge 17*; Verlag Gustav Fischer: Jena, Germany, 1930; p. 111.
56. Schwarz, H.-U. Zur Sedimentologie und Fazies des Unteren Muschelkalkes in Südwestdeutschland und angrenzenden Gebieten. Ph.D. Thesis, Eberhard-Karls-Universität Tübingen, Tübingen, Germany, 1970, unpublished.
57. Vossmerbäumer, H. Organosedimentäre Gefüge im oberen Wellenkalk (mu3, Trias) Frankens. *Neues Jahrb. Geol. Paläontol. Mon.* **1971**, 437–448.
58. Hagdorn, H.; Simon, T. Rinnenbildung und Emersion in den Basisschichten des Mittleren Muschelkalks von Eberstadt (Nordbaden). *Neues Jahrb. Geol. Paläontol.* **1993**, *189*, 119–145.

59. Krause, T.; Weller, H. Aufbau und palökologische Bedeutung der Stromatolithe im Übergang vom Mittleren zum Oberen Muschelkalk der Thüringer Mulde. *Beitr. Geol. Thüring.* **2000**, *7*, 147–193.
60. Bachmann, G.H.; Gwinner, M.P. *Algen-Stromatolithen von der Grenze Unterer/Mittlerer Keuper (Obere Trias) bei Schwäbisch Hall (Nordwürttemberg, Deutschland)*. *Neues Jahrbuch für Geologie und Paläontologie, Monatshefte*; Geologisch-Paläontologisches Institut der Technischen Hochschule Stuttgart: Stuttgart, Germany, 1971; pp. 594–604.
61. Bachmann, G.H. A lamellibranch-stromatolite bioherm in the Lower Keuper (Ladinian, Middle Triassic), South Germany. *Facies* **2002**, *46*, 83–88. [[CrossRef](#)]
62. Scotese, C.; Mc Kerrow, W.S. Revised World maps and introduction. *Geol. Soc. Lond. Mem.* **1990**, *12*, 1–21. [[CrossRef](#)]
63. Ziegler, P.A. *Geological Atlas of Western and Central Europe*; Geological Society Publishing House: Bath, UK, 1990; pp. 1–239.
64. Stampfli, G.M. Tethyan oceans. In *Tectonics and Magmatism in Turkey and the Surrounding Area*; Bozkurt, E., Winchester, J.A., Piper, J.D.A., Eds.; Special Publications 173; Geological Society: London, UK, 2000; pp. 1–23.
65. Hagdorn, H. Paläobiogeographie des Mitteleuropäischen Beckens in der Frühen und Mittleren Trias und Faunenimmigration ins Muschelkalkmeer. *Schr. Dtsch. Ges. Geowiss.* **2020**, *91*, 111–123.
66. Simon, T.; Hagdorn, H.; Dittrich, D.; Röhling, S.; Voigt, T. Lithostratigraphie der Mittlerer-Muschelkalk-Subgruppe. *Schr. Dtsch. Ges. Geowiss.* **2020**, *91*, 441–466.
67. Bishop, J.W.; Osleger, D.A.; Montanez, I.; Sumner, D. Meteoric diagenesis and fluid-rock interaction in the Middle Permian Capitan backreef: Yates Formation, Slaughter Canyon, New Mexico. *AAPG Bull.* **2014**, *98*, 1495–1519. [[CrossRef](#)]
68. Craig, H. Isotopic Variations in Meteoric Waters. *Science* **1961**, *133*, 1702–1703. [[CrossRef](#)] [[PubMed](#)]
69. Hauck, T.E.; Corlett, H.J.; Grobe, M.; Walton, E.L.; Sansjofre, P. Meteoric diagenesis and dedolomite fabrics in precursor primary dolomicrite in a mixed carbonate-evaporite system. *Sedimentology* **2018**, *65*, 1827–1858. [[CrossRef](#)]
70. Awramik, S.; Margulis, L.; Barghoorn, E. Chapter 4.4 Evolutionary Processes in the Formation of Stromatolites. *Dev. Sedimentol.* **1976**, *20*, 149–162.
71. Reitner, J. Microbial mats. In *Encyclopedia of Geobiology*; Reitner, J., Thiel, V., Eds.; Springer: Berlin/Heidelberg, Germany, 2011; pp. 606–608.
72. Suarez-Gonzalez, P.; Reitner, J. Ooids forming in situ within microbial mats (Kiritimati atoll, central Pacific). *PalZ* **2021**, *95*, 809–821. [[CrossRef](#)]
73. Suarez-Gonzalez, P.; Benito, M.; Quijada, I.; Mas, R.; Campos-Soto, S. ‘Trapping and binding’: A review of the factors controlling the development of fossil agglutinated microbialites and their distribution in space and time. *Earth Sci. Rev.* **2019**, *194*, 182–215. [[CrossRef](#)]
74. Olivier, N.; Brayard, A.; Vennin, E.; Escarguel, G.; Fara, E.; Bylund, K.G.; Jenks, J.F.; Caravaca, G.; Stephen, D.A. Evolution of depositional settings in the Torrey area during the Smithian (Early Triassic, Utah, USA) and their significance for the biotic recovery. *Geol. J.* **2016**, *51*, 600–626. [[CrossRef](#)]
75. Olivier, N.; Fara, E.; Vennin, E.; Bylund, K.G.; Jenks, J.F.; Escarguel, G.; Stephen, D.A.; Goudemand, N.; Snyder, D.; Thomazo, C.; et al. Late Smithian microbial deposits and their lateral marine fossiliferous limestones (Early Triassic, Hurricane Cliffs, Utah, USA). *Facies* **2018**, *64*, 13. [[CrossRef](#)]
76. Adachi, N.; Asada, Y.; Ezaki, Y.; Liu, J. Stromatolites near the Permian–Triassic boundary in Chongyang, Hubei Province, South China: A geobiological window into palaeo-oceanic fluctuations following the end-Permian extinction. *Palaeogeogr. Palaeoclim. Palaeoecol.* **2017**, *475*, 55–69. [[CrossRef](#)]
77. Murray, J.W.; Wright, C.A. The Carboniferous Limestone of Chipping Sodbury and Wick, Gloucestershire. *Geol. J.* **1971**, *7*, 255–270. [[CrossRef](#)]
78. Reitner, J. Modern cryptic microbialite/metazoan facies from Lizard Island (Great Barrier Reef, Australia) formation and concepts. *Facies* **1993**, *29*, 3–39. [[CrossRef](#)]
79. Reitner, J.; Gautret, P.; Marin, F.; Neuweiler, F. Automicrite in a modern marine microbialite: Formation model via organic matrices (Lizard Island, Great Barrier Reef, Australia). *Bull. Inst. Océanogr.* **1995**, *4*, 237–263.
80. Preto, N.; Breda, A.; Corso, J.D.; Spötl, C.; Zorzi, F.; Frisia, S. Primary dolomite in the Late Triassic Travenanzes Formation, Dolomites, Northern Italy: Facies control and possible bacterial influence. *Sedimentology* **2015**, *62*, 697–716. [[CrossRef](#)]
81. Warthmann, R.; Van Lith, Y.; Vasconcelos, C.; Mc Kenzie, J.A.; Karpoff, A.M. Bacterially induced dolomite precipitation in anoxic culture experiments. *Geology* **2000**, *28*, 1091–1094. [[CrossRef](#)]
82. Liu, D.; Fan, Q.; Papineau, D.; Yu, N.; Chu, Y.; Wang, H.; Qiu, X.; Wang, X. Precipitation of protodolomite facilitated by sulfate-reducing bacteria: The role of capsule extracellular polymeric substances. *Chem. Geol.* **2020**, *533*, 119415. [[CrossRef](#)]
83. Reitner, J.; Schumann-Kindel, G. Pyrite in mineralized sponge tissue—Product of sulfate reducing sponge related bacteria? *Facies* **1997**, *36*, 272–284.
84. Schumann-Kindel, G.; Bergbauer, M.; Manz, W.; Szewzyk, U.; Reitner, J. Aerobic and anaerobic microorganisms in modern sponges: A possible relationship to fossilization-processes. *Facies* **1997**, *36*, 268–272.
85. Hoffmann, F.; Larsen, O.; Thiel, V.; Rapp, H.T.; Pape, T.; Michaelis, W.; Reitner, J. An Anaerobic World in Sponges. *Geomicrobiol. J.* **2005**, *22*, 1–10. [[CrossRef](#)]
86. Zhang, D.; Sun, W.; Feng, G.; Zhang, F.; Anbuezhian, R.; Li, Z.; Jiang, Q. Phylogenetic diversity of sulphate-reducing *Desulfovibrio* associated with three South China Sea sponges. *Lett. Appl. Microbiol.* **2015**, *60*, 504–512. [[CrossRef](#)] [[PubMed](#)]

87. Benton, M.J.; Twitchett, R.J. How to kill (almost) all life: The end-Permian extinction event. *Trends Ecol. Evol.* **2003**, *18*, 358–365. [[CrossRef](#)]
88. Wignall, P.B. The End-Permian mass extinction—How bad did it get? *Geobiology* **2007**, *5*, 303–309. [[CrossRef](#)]
89. Chen, Z.-Q.; Benton, M. The timing and pattern of biotic recovery following the end-Permian mass extinction. *Nat. Geosci.* **2012**, *5*, 375–383. [[CrossRef](#)]
90. Payne, J.L.; Clapham, M.E. End-Permian Mass Extinction in the Oceans: An Ancient Analog for the Twenty-First Century? *Annu. Rev. Earth Planet. Sci.* **2012**, *40*, 89–111. [[CrossRef](#)]